

# Unsupervised Domain Adaptation for Retinal Vessel Segmentation with Adversarial Learning and Transfer Normalization

Wei Feng, Lie Ju, Lin Wang, Kaimin Song, Xin Wang, Xin Zhao, Qingyi Tao, and Zongyuan Ge

**Abstract**—Retinal vessel segmentation plays a key role in computer-aided screening, diagnosis, and treatment of various cardiovascular and ophthalmic diseases. Recently, deep learning-based retinal vessel segmentation algorithms have achieved remarkable performance. However, due to the domain shift problem, the performance of these algorithms often degrades when they are applied to new data that is different from the training data. Manually labeling new data for each test domain is often a time-consuming and laborious task. In this work, we explore unsupervised domain adaptation in retinal vessel segmentation by using entropy-based adversarial learning and transfer normalization layer to train a segmentation network, which generalizes well across domains and requires no annotation of the target domain. Specifically, first, an entropy-based adversarial learning strategy is developed to reduce the distribution discrepancy between the source and target domains while also achieving the objective of entropy minimization on the target domain. In addition, a new transfer normalization layer is proposed to further boost the transferability of the deep network. It normalizes the features of each domain separately to compensate for the domain distribution gap. Besides, it also adaptively selects those feature channels that are more transferable between domains, thus further enhancing the generalization performance of the network. We conducted extensive experiments on three regular fundus image datasets and an ultra-widefield fundus image dataset, and the results show that our approach yields significant performance gains compared to other state-of-the-art methods.

**Index Terms**—Retinal vessel segmentation, Domain adaptation, Batch normalization, Ultra-wide field fundus images.

## I. INTRODUCTION

VESSEL analysis in retinal fundus images is one of the most important tools for screening, diagnosis, and treatment of many ocular, hypertension, and cardiovascular diseases [1]. For example, diabetic retinopathy can cause

(Corresponding author: Zongyuan Ge)

Wei Feng, Lin Wang, Kaimin Song are with the Monash-Airdoc joint research group, Monash University, Clayton, VIC 3800 Australia (E-mail: wf02429, wanglin.mailbox, kims75699@gmail.com).

Lie Ju and Zongyuan Ge are with Monash University, Clayton, VIC 3800 Australia. Lie Ju and Zongyuan Ge are also with Airdoc, Beijing 100089, China (E-mail: julie334600@gmail.com, zongyuan.ge@monash.edu).

Qingyi Tao is with NVIDIA AI Technology Center, Singapore (E-mail: qtao002@e.ntu.edu.sg).

Xin Zhao and Xin Wang are with Airdoc, China (E-mail: zhaoxin, wangxin@airdoc.com).

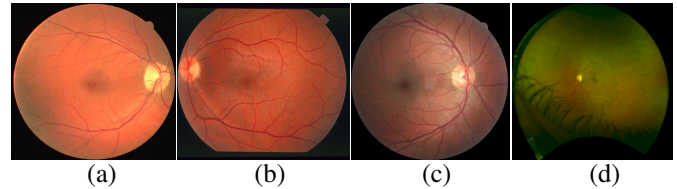


Fig. 1. Exemplar fundus images from different fundus datasets. From left to right are (a)DRIVE; (b)STARE; (c)our clinical dataset; (d)ultra-wide field fundus image dataset. It can be observed that there is a distinct visual appearance between different fundus datasets.

neovascularization, hypertension can cause vessel curvature, and stroke and atherosclerosis can cause structural changes in vessel morphology [2]. Accurate retinal vessel segmentation is crucial for subsequent vessel morphology analysis [3]. Recently, deep learning-based approaches have made significant progress for automated retinal vessel segmentation tasks [4], [5]. However, a high-performance deep learning model usually relies on a large number of training samples with corresponding annotations. This is impractical in the field of medical imaging, especially for retinal vessel segmentation. Even for experienced clinicians, manually annotating a binary vessel map is very time-consuming and labor-intensive. For example, it typically takes 18 hours to fully annotate an ultra-widefield (UWF) fundus image. Therefore, it is of importance to explore the use of fundus images from other modalities for scalable and robust modeling [6].

However, fundus images from different sources have distinct visual appearance. As shown in Fig. 1, these differences in visual appearance are due to differences in imaging devices and imaging protocols. This is common in practical clinical scenarios. Even fundus images obtained from the same fundus camera may show variation because of the differences in clinical settings and subjects. In addition, the range of imaging and resolution of these fundus images from different sources may also differ. For example, the regular fundus images in Fig. 1(a)–(c) have an imaging angle of only  $20^{\circ}$ – $60^{\circ}$  and can only cover a small part of the central retinal area, which prevents physicians from adequately identifying many common fundus diseases due to the lack of peripheral fundus angiography imaging. In contrast, the UWF fundus image in Fig. 1(d) can be obtained at  $200^{\circ}$ , allowing imaging of approximately 80% of the retinal fundus. In addition, it can show both posterior pole and peripheral retinal images without dilating the patient’s pupil, which can reveal occult

peripheral retinal ischemia or neovascularisation, thus more effectively guiding relevant treatment plans and expanding clinicians' knowledge of the peripheral retina [7]. However, these differences between fundus datasets will lead to substantial performance degradation when transferring a deep learning model trained on one fundus dataset to another, since a high-performance deep learning model requires that the train data and test data are drawn from the same distribution [8].

To address these challenges mentioned above, this paper proposes a new unsupervised domain adaptation framework with adversarial learning and transfer normalization for cross-domain retinal vessel segmentation. Specifically, We first propose an entropy-based adversarial learning strategy to align the entropy of the predicted outputs from the source and target domains, which has two benefits: (1) reducing the distribution gap between the source and target domains, thus enabling the model trained with the source domain data to generalize well on the unlabeled target domain; (2) achieving the goal of minimizing the entropy on the target domain, forcing the model to produce confident predictions for unlabeled data from the target domain. Our motivation stems from the observation that models trained on labeled source domain data tend to produce high confidence predictions on source domain data and low confidence predictions on target domain data due to domain distribution differences. Here, we employ Shannon Entropy [9] to model prediction uncertainty, with a high confidence prediction implies a low entropy value and a low confidence prediction implies a high entropy value. We argue that it would be a possible solution to compensate for domain distribution differences to use adversarial learning by aligning entropy maps between domains, thereby encouraging models to produce high confidence (low entropy) predictions on unlabeled target domain data as well.

In addition, to further improve the network transferability, a transfer normalization layer is proposed to replace the batch normalization (BN) layer in deep neural network (DNN) for domain adaptation setting. The transfer normalization layer normalizes feature representations from different domains separately, which can compensate for the discrepancies between domains. At the same time, since different feature channels capture different patterns, they have different transferability, and thus need careful modulated during the adaptation process. To this end, we use the statistics obtained from the BN layer to measure the transferability of different feature channels between the source and target domains, and then adaptively reweight each feature channel so that feature channels with higher transferability can be emphasized, and those with lower transferability are suppressed, which enables further enhancing the generalization performance of the model on the target domain. The main contributions of this paper are as follows:

- 1) We propose a new unsupervised domain adaptation framework for cross-domain retinal vessel segmentation. An entropy-based adversarial training strategy is developed to reduce the domain gap between the source and target domains, thus improving the generalization performance of the model on the target domain. Besides, it achieves the goal of entropy minimization and thus encourages the model to produce high confidence predic-

tions on the target domain.

- 2) To further enhance the network's transferability, we propose a transfer normalization layer which normalizes the feature representations of two domains separately to explicitly compensates for the inter-domain differences. We also quantified the transferability of each feature channel and adaptively reweighted them, thus a further improvement on the generalization performance of the network was observed.
- 3) To the best of our knowledge, this is the first work that explores the use of regular fundus datasets to aid in UWF retinal vessel segmentation. Our method can detect most of the retinal vessels in UWF fundus images without any annotation on the target dataset.
- 4) We evaluated our method on three regular fundus datasets and a UWF fundus dataset. The experimental results show that our method not only yields significant performance gains on transfer tasks between regular fundus datasets, but also outperforms other state-of-the-art methods by a large margin on the more challenging transfer tasks between regular and UWF fundus datasets.

## II. RELATED WORK

### A. Retinal vessel segmentation

The existing retinal vessel segmentation can be divided into two main branches: unsupervised methods and supervised methods. Unsupervised methods use heuristics knowledge about retinal vessels to identify blood vessels, mainly including the shape of the vessels, the position of the optic cup and optic disc, and the centerline of the vessels, etc. Methods derived from this heuristic knowledge include matched filter [10], vessel tracking [11], morphological processing [12], etc. However, the acquisition of such heuristic knowledge is very challenging and subjective, and the generalization performance of these methods is also very poor in practical clinical application scenarios [13]. Supervised learning methods mainly include traditional machine learning methods and deep learning methods. Traditional machine learning methods use the labeled retinal vessel image dataset and hand-crafted features to build segmentation models. For example, Soares et al. [14] extracted hand-crafted features using a 2-D Gabor filter and then used a Bayesian network to classify each pixel in the image. Roychowdhury et al. [15] extracted digital morphological features of vessel regions and background regions and then used Gaussian mixture model (GMM) for classification. However, the performance of these methods relies heavily on the quality of the manually extracted features. Deep learning methods are capable of automatically extracting features from the original fundus image and are able to perform vessel segmentation in an end-to-end manner. For example, Yan et al. [16] proposed a new segmentation loss to balance the importance between thick and thin vessels during training and thus better segment fine vessels. Son et al. [17] introduced a generative adversarial network to produce more accurate and clearer vessel maps, and the experimental results demonstrated that their method could generate fewer false predictions on fine vessels. Sun et al. [18] developed a channel-wise stochastic

gamma correction and a channel-wise stochastic vessel augmentation technique to encourage the model to learn invariant and more discriminative features. However, all of the above methods require a large amount of annotated training data to train a high-performance vessel segmentation model, and the trained models are difficult to generalize across different fundus datasets due to the domain shift. In this work, we focus on unsupervised domain adaptation in retinal fundus vessel segmentation, leveraging annotated source fundus datasets to build a robust segmentation model that generalizes well over unannotated target fundus datasets with domain shift.

### B. Domain adaptation

Domain adaptation aims to bridge the distribution gap between the source and target domains so that the model can generalize well across domains. In this paper, we focus on deep learning-based domain adaptation methods. Previous deep domain adaptation methods generally fall into two main categories: moment matching and adversarial training [19]. Moment matching aims at aligning the feature distributions of the source and target domains by minimizing the difference between the distributions of the two domain data in the high-dimensional feature space [19], [20]. Adversarial training is derived from the idea of generative adversarial network (GAN), where generator and discriminator boost each other by establishing a two-player min-max competition game mechanism [21], [22]. Domain adaptation has achieved impressive performance in several areas such as computer vision and natural language processing [22]. However, in the field of retinal vessel segmentation, domain adaptation has rarely been studied. Mehran et al. [23] proposed a domain adaptation network based on adversarial learning for cross-domain retinal vessel segmentation. Zhuang et al. [24] proposed an asymmetrical maximum classifier discrepancy (AMCD) approach for cross-domain retinal vessel segmentation.

However, these methods only evaluated the performance on the transfer tasks between limited regular fundus datasets and did not consider transfer tasks between regular fundus datasets and UWF fundus datasets. UWF images have more valuable clinical applications than regular fundus images [7]. However, models trained with regular fundus images may not be able to accurately identify peripheral vessels and some lesions in UWF fundus images due to the difference in imaging range. In addition, UWF images contain more noise interference such as eyelashes, eyelids, and lesions, which leads to the much higher cost of labeling UWF images. Therefore, it is of interest to investigate how to utilize regular fundus image datasets with rich annotation to assist in the annotation of UWF fundus datasets. To our best knowledge, we are the first attempt to utilize regular fundus images to perform UWF vessel segmentation without any annotations of UWF fundus images. Our approach was able to identify most retinal vessels of the UWF fundus images and achieved consistent performance gains in all evaluation metrics.

### C. Batch normalization

Batch normalization (BN) [25] is one of the most successful inventions in deep neural networks. It can accelerate network

training and alleviate the problem of internal covariance shift during the training process [26]. However, the traditional BN layer may not be suitable for the domain adaptation problem because it combines the source and target domain data into a single batch and feeds the combined data to the BN layer during training so that the statistics (mean and variance) of the BN layer are estimated on the data of both domains without considering which domain the feature representation comes from. However, due to domain shift [27], the distribution of source and target domain are different, which means that their distribution statistics (mean and variance) are also different. In this case, the traditional BN layer may distort the feature distribution and worsen the network's transferability. Some research work has been done to address this issue. For example, Li et al. [28] proposed a simple yet effective strategy for domain adaptation problem by replacing the statistics of each BN layer in the source domain with the statistics of the target domain. Liu et al. [29] proposed a domain-specific batch normalization layer by normalizing the features of each domain separately during the training process for improving the performance of prostate segmentation. However, these methods do not explore the transferability among each channel of different domains. Since some feature channels learn domain shared patterns that should be emphasized, while some feature channels may learn non-shared patterns, such as background or noise, etc., and thus should be suppressed. In this paper, we measure the similarity of different feature channels across domains by the mean and variance estimated in the BN layer so that each feature channel can be reweighted adaptively. Feature channels with higher domain relevance will be highlighted, while those with lower domain relevance will be repressed, thus further enhancing the transferability of the network.

## III. METHODOLOGY

Fig. 2 demonstrates the overview of our proposed framework for unsupervised domain adaptation in retinal vessel segmentation, which performs domain adaptation between two fundus image datasets from different sources by an entropy-based adversarial training method and a transfer normalization layer. The entropy-based adversarial training strategy can reduce domain differences while adjusting the model to produce confident predictions on unlabeled target fundus images. The transfer normalization layer can further improve the generalization performance of the network.

### A. Entropy-based Adversarial Learning

In this work, we follow the principle of adversarial training and propose an entropy-based adversarial learning strategy to train our domain adaptation framework. The spirit of adversarial learning stems from generative adversarial networks [21], which consists of two modules: a generator and a discriminator, where the generator learns to capture the distribution of real data while the discriminator tries to distinguish the generated data from the real data. The two networks are alternately optimized until the data generated by the generator can fool the discriminator.

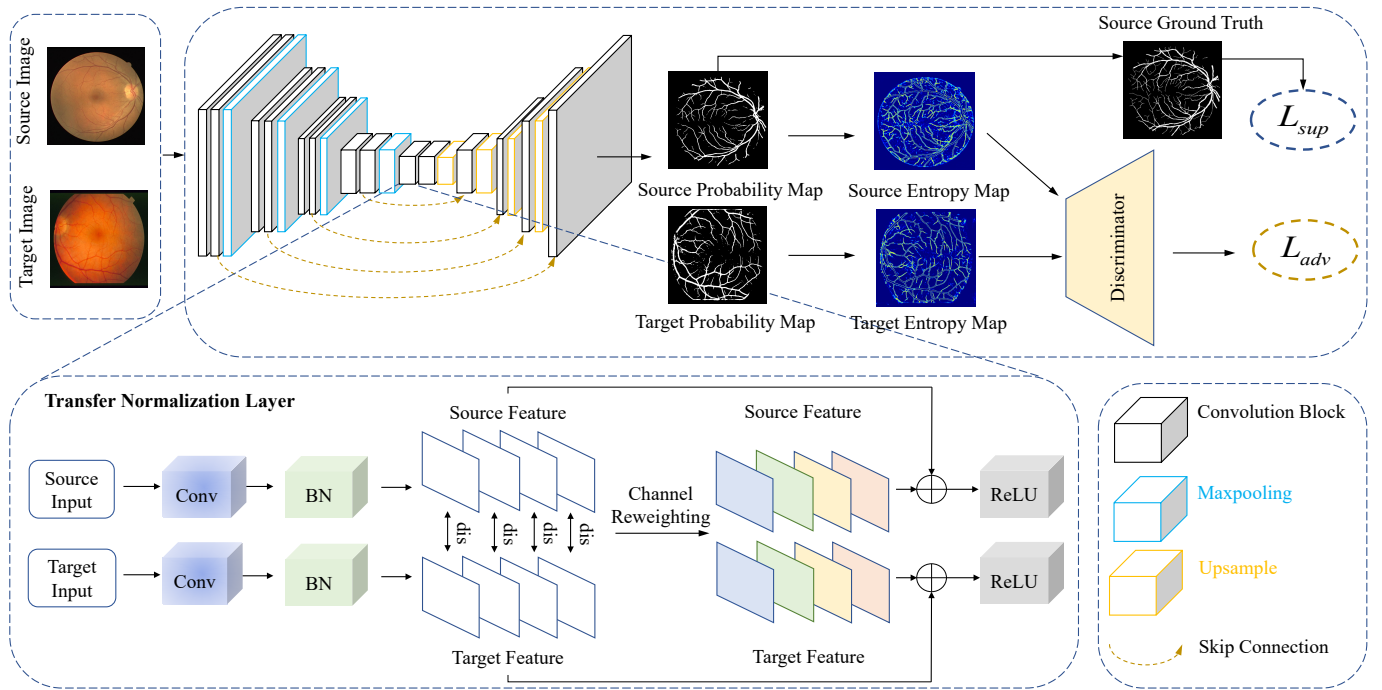


Fig. 2. The overview of our proposed framework for unsupervised domain adaptation in retinal vessel segmentation. It uses an entropy-based adversarial learning strategy to bridge the domain distribution discrepancy while prompting the model to produce confident predictions on the unlabeled target domain data. In addition, a new transfer normalization layer is proposed to normalize the feature representation of each domain separately while adaptively reweighting each feature channel to further enhance the generalization performance of the model.

Specifically, given the labeled source domain fundus dataset  $D^s = \{(x_i^s, y_i^s)\}_{i=1}^{N_s}$  and the unlabeled target domain fundus dataset  $D^t = \{x_i^t\}_{i=1}^{N_t}$ , where  $x_i^s \in \mathbb{R}^{H \times W \times 3}$  and  $x_i^t \in \mathbb{R}^{H \times W \times 3}$  denote the  $i$ -th sample of the source domain and target domain, and  $y_i^s \in \{0, 1\}^{H \times W}$  is the corresponding ground truth label. We feed the source and target domain data into a segmentation network  $F$  and obtain the predicted probability maps  $P^s \in \mathbb{R}^{H \times W \times C}$  and  $P^t \in \mathbb{R}^{H \times W \times C}$  for each domain,  $C = 2$  is the number of categories. We then generate the entropy map  $I^s$  and  $I^t$  based on the probability maps for each domain:

$$\begin{aligned} I^s &= -\frac{1}{\log(C)} \sum_{c \in \{0,1\}} P_c^s \log P_c^s, \\ I^t &= -\frac{1}{\log(C)} \sum_{c \in \{0,1\}} P_c^t \log P_c^t. \end{aligned} \quad (1)$$

A discriminator network  $D$  is then constructed to distinguish the entropy maps from the two domains. Unlike previous work [22], we use the entropy map rather than the original prediction probability map as the input to the discriminator. This is because models trained on labeled source domain data tend to give over-confident (low-entropy) predictions for source domain data and under-confident (high-entropy) predictions for unlabeled target domain data. Therefore, we believe that by aligning the entropy map between domains with adversarial training can encourage the model to give confident predictions on unlabeled target domain data and reduce the distribution differences between domains so that the segmentation model generalizes well on the target domain. The discriminator uses a binary cross-entropy loss to classify the entropy maps of the

source and target domains, which can be formulated as:

$$L_d = -\sum_{k \in \mathcal{V}} (1-z) \log(D(I_k^s)) + z \log(D(I_k^t)), \quad (2)$$

where  $\mathcal{V} = \{1, 2, \dots, H \times W\}$  denotes all pixels in the fundus image, and  $z = 0$  if the entropy map comes from the source domain and  $z = 1$  if the entropy map comes from the target domain.

For the segmentation network, we expect the distribution of  $I^t$  to be close to  $I^s$ . The optimization objective of the segmentation network can be formulated as:

$$\begin{aligned} L_{seg} &= L_{sup} + \lambda_d L_{adv} \\ &= -\sum_{k \in \mathcal{V}} \sum_{c \in \{0,1\}} P_{k,c}^s \log(y_{k,c}^s) - \lambda_d \sum_{k \in \mathcal{V}} \log(D(I_k^t)), \end{aligned} \quad (3)$$

where  $L_{sup}$  is the supervised loss on the labeled source domain samples and  $L_{adv}$  is the adversarial loss.  $\lambda_d$  is a hyperparameter to balance these two loss terms, which is fixed as  $1e-3$  in our setting.

## B. Transfer Normalization

Batch normalization (BN) [25] is widely used in deep neural networks to accelerate network convergence and reduce internal covariance shift. Recent studies have shown that the essence of BN works due to its ability to make the loss landscape smoother [26]. Specifically, let  $h_m \in [h_1, h_2, \dots, h_M]$  denote one of the  $M$  feature channels at a certain layer of the deep network, BN first calculates the mean and variance of  $h_m$  over a mini batch of data, i.e.  $E[h_m]$  and  $\text{Var}[h_m]$ , each feature



channel is then transformed to zero mean and unit variance using this mean and variance. To enhance the representation capability of the model, two additional learnable parameters  $\gamma$  and  $\beta$  are introduced to scale and shift each normalized feature channel:

$$o_m = \gamma_m \hat{h}_m + \beta_m, \quad \hat{h}_m = \frac{h_m - E[h_m]}{\sqrt{\text{Var}[h_m] + \epsilon}}, \quad (4)$$

where  $\epsilon$  is an infinitesimal to ensure numerical stability.

However, in our problem setting, the imaging devices, imaging protocols, range of imaging, and resolution vary across different fundus datasets, resulting in significant differences between the feature distributions of different fundus datasets, which is often also referred to as the domain shift phenomenon [27]. The traditional BN layer combines data from different domains into a single batch and then normalizes this single batch, which may lead to two issues: (1) due to domain distribution gap, the sharing of mean and variance among different domains in the BN layer may distort the feature distribution and deteriorate the transferability of the network, making it difficult for the network to learn generic and robust features; (2) during the training phase, the BN layer estimates global mean and variance on the single batch consisting of data from different domains, which may be inaccurate and may cause performance degradation when used directly for normalization of target domain data during the testing phase.

To address the above issues, we propose a transfer normalization layer to replace the BN layer for the domain adaptation problem. Specifically, let  $h_m^s \in [h_1^s, h_2^s, \dots, h_M^s]$  and  $h_m^t \in [h_1^t, h_2^t, \dots, h_M^t]$  denote a certain feature channel of the feature map from the source and target domain, and we normalize the feature channel for each domain separately as follows:

$$\begin{aligned} o_m^s &= \gamma_m^s \hat{h}_m^s + \beta_m^s, & \hat{h}_m^s &= \frac{h_m^s - E[h_m^s]}{\sqrt{\text{Var}[h_m^s] + \epsilon}}, \\ o_m^t &= \gamma_m^t \hat{h}_m^t + \beta_m^t, & \hat{h}_m^t &= \frac{h_m^t - E[h_m^t]}{\sqrt{\text{Var}[h_m^t] + \epsilon}}, \end{aligned} \quad (5)$$

where  $[\gamma^s, \beta^s]$  and  $[\gamma^t, \beta^t]$  are the learnable parameters of the source and target domains, respectively.

Meanwhile, for the domain adaptation problem, since the patterns captured by different feature channels are different, some feature channels may capture patterns shared among both domains, while others capture domain-specific patterns. Therefore, a heuristic question is: Can we quantify the transferability of different feature channels and thus enhance the transferability of the network in some way? In this paper, we provide a solution by reusing the statistics computed by the BN layer on the feature representation of each domain to automatically select those feature channels that are more transferable. Specifically, we first compute the distance between each channel of the source and target domains as follows:

$$d_m = \left| \frac{E[h_m^s]}{\sqrt{\text{Var}[h_m^s] + \epsilon}} - \frac{E[h_m^t]}{\sqrt{\text{Var}[h_m^t] + \epsilon}} \right|, \quad (6)$$

$d$  quantifies the transferability of each feature channel, then we use Student t-distribution [30] with one degree of freedom to

convert the computed distance into probability  $\eta$  to adaptively reweight each feature channel:

$$\eta_m = \frac{M(1 + d_m)^{-1}}{\sum_{j=1}^M (1 + d_j)^{-1}}, \quad (7)$$

where  $M$  is the number of feature channels in a layer of the network. Moreover, to avoid over-penalizing those informative channels, we further introduce a residual mechanism [31] to combine the normalized and reweighted feature channels to form the final output:

$$\hat{o}^s = (1 + \eta)o^s, \quad \hat{o}^t = (1 + \eta)o^t. \quad (8)$$

Using this distance-based probability to quantify the transferability of each feature channel, those channels with higher transferability will be assigned with greater importance, while those with lower transferability will be assigned with lower weights. This mechanism allows the network to better learn domain shared features while suppressing the interference of those non-essential domain-specific variations.

## IV. EXPERIMENTS

To validate the effectiveness of our proposed method, we perform experiments on two types of transfer tasks: (1) transfer tasks between several regular fundus datasets; (2) transfer tasks between regular fundus datasets and UWF fundus dataset, which is a more challenging transfer task.

### A. Datasets

We conducted experiments on three regular fundus datasets (DRIVE, STARE, a regular fundus dataset obtained from a private hospital) and a UWF fundus dataset (PRIME-FP20). The details of each fundus dataset are as follows.

The DRIVE (digital retinal images for vessel extraction) dataset [32] is a database of retinal images constructed by the Diabetic Retinopathy Screening Group in the Netherlands, which was derived from 400 diabetic patients aged 20-90 years. It contains a total of 40 retinal images, 33 of which have no diabetic retinopathy, and the remaining 7 have diabetic retinopathy. All images were acquired with a CannonCR5 astigmatism-free 3CCD camera with an acquisition angle of 45° and a resolution of 584 × 565. The dataset contains a training subset and a test subset, each with 20 images. Each training image is equipped with a manually annotated binary vessel map as the ground truth label, and each test image is equipped with two manually annotated binary vessel maps, one for the ground truth label and one for the human observer's results.

The STARE (structured analysis of the retinal) dataset [33] contains 20 retinal fundus images, 10 of which have no retinal fundus lesions, and the remaining 10 have retinal fundus lesions. Each image was taken with the TopCon TRV-5 fundus camera at an angle of 35° and a resolution of 700 × 605. Each image has two manually labeled binary vessel maps by human experts, where the first one is usually used as the ground truth label. Since there is no official split for this dataset, we use the first ten images for training and the remaining ten images for testing.

Retinal40 is a regular fundus dataset obtained from a private hospital. It contains 40 regular fundus images, 30 of which have no retinal fundus lesions and 10 of which have retinal fundus lesions. Each fundus image was acquired with a 45° fundus camera (Type CR6-45NM, Canon Inc, Lake Success, NY, United States). We resize each image to  $1024 \times 1024$  pixels. Each fundus image was annotated by a human annotator using ImageJ software [34] with the segmentation editor plugins to annotate the ground truth labels. The annotator repeatedly adjusted the image illumination and contrast to accurately label the retinal vessels in the fundus images. We also provide a binary mask for the FOV of each fundus image. We use the first 30 images for training and the remaining 10 images for testing.

The PRIME-FP20 dataset [35] contains 15 pairs of simultaneously captured UWF-FP and UWF-FA images. In this paper, we only use UWF-FP images. All images were captured using the Optos California and 200Tx cameras (Optos plc, Dunfermline, United Kingdom). Each image has a resolution of  $4000 \times 4000$  pixels and is stored in 8-bit TIFF format. Each UWF FP was equipped with a binary vessel map labeled by a human expert and a binary mask to distinguish fundus regions from non-fundus regions. We use the first ten images for training and the remaining five images for testing.

### B. Pre-processing and Implementation Details

Since different fundus datasets have different illumination, contrast, and resolution, to compensate for this variation, we first convert each image to grayscale, then normalize it to zero mean and unit variance, and finally map it to  $[0, 255]$ . We also use Contrast Limited Adaptive Histogram Equalization (CLAHE) [36] to further improve the contrast and suppress noise in the fundus images. Specifically, we divide each fundus image into several  $8 \times 8$  regions and then perform histogram equalization on each small region individually. Compared with the traditional histogram equalization method, CLAHE is more suitable for improving the local contrast and enhancing the image edge information. In addition, following our previous work [7], we removed artifacts in the UWF fundus images, such as eyelids and eyelashes, using a UNet [37] segmentation network.

We construct two types of transfer tasks, i.e., transfer tasks between the regular fundus dataset and transfer tasks between the regular fundus and UWF fundus datasets. For each transfer task, we train the segmentation model using all the labeled source-domain fundus images and the unlabeled target-domain training images, and then evaluate the performance of the model using the testset of the target domain, noting that we only use the testset of target-domain in the testing phase. For example, for the transfer task *DRIVE*  $\rightarrow$  *STARE*, we train the segmentation model using 40 labeled fundus images of *DRIVE*(source domain) and ten unlabeled training images of *STARE*(target domain), and then evaluate the model performance on the testset of *STARE* .

For model training, following previous work [5], we use the patch-based training approach. Specifically, we randomly extract 10,000  $64 \times 64$  patches from each fundus image in each

fundus dataset for model training, so the number of patches of each dataset are: *DRIVE* (400,000), *STARE* (200,000), *Retinal40* (400,000), and *UWF* (150,000), respectively. In the test phase, we also use a patch-based evaluation strategy. Specifically, we extract partially overlapping patches from each test image in both directions with a stride of 10 in an orderly manner, and each patch has a size of  $64 \times 64$ . We then feed the extracted patches into the segmentation network to obtain the prediction probability map. Since the patches are partially overlapping, some pixels may appear in multiple patches, so we further average the prediction probability of each pixel to obtain the final binary vessel prediction map. During the training phase, to alleviate the overfitting phenomenon and further improve the generalization performance of the model, we also use some data augmentation techniques, including: random horizontal/vertical flipping, random rotation at an angle from  $[90^\circ, 180^\circ, 270^\circ]$  [5].

We adopted UNet [37] as the segmentation network for its superior performance in several medical image processing tasks. Unlike the original UNet, we replace the BN layer following each convolutional layer with our proposed transfer normalization layer for the domain adaptation problem. In addition, for the discriminator network, we use a structure similar to DCGAN [38]. Specifically, it contains four convolutional layers, each followed by a leaky ReLU activation layer, and finally the discriminator outputs the probability that the input belongs to the source and target domains. We use the Adam algorithm [39] to optimize the segmentation network and discriminator network, with the learning rate set to  $1e-3$  and the weight decay set to  $3e-4$  for the segmentation network, and  $1e-4$  for the learning rate of the discriminator network. The batch size is 256, and the number of iterations is 50,000. To schedule the learning rate, we apply a polynomial decay to the learning rate of the segmentation network and the discriminator [40]. All models are implemented based on the PyTorch deep learning framework [41], and are trained and evaluated on four 1080Ti GPUs. Following [5], we adopt six metrics to evaluate the performance of our proposed approach, including: the area under the receiver operating characteristics curve (AUC), area under the precision-recall curve (AUPR), F1 score (F1), sensitivity (SE), specificity (SP), and accuracy (ACC) to evaluate the performance of different algorithms.

### C. Results

1) *Evaluations on the Transfer Tasks Regular  $\rightarrow$  Regular*: We compare our proposed algorithm with the baseline model, i.e., model trained with source domain data only and then tested on unlabeled target domain data, and five state-of-the-art deep domain adaptation methods, including: DANN [23], AdaptSeg [22], AdaBN [28], AMCD [24], and DSBN [29]. DANN introduces a discriminator network to distinguish between source and target domain feature representations, while the segmentation network learns a domain invariant feature to fool the discriminator. AdaptSeg employs adversarial learning in the output space to bridge domain distribution gaps. AdaBN substitutes the statistics of the BN layer with those of the target domain during the testing phase for domain adaptation

scenarios. AMCD adapts the target features by aligning the predicted outputs of two different classifiers. DSBN allocates a BN layer to each domain to compensate for inter-domain distribution differences. For fair comparison, these comparison algorithms all use UNet as the backbone network.

Fig. 3 presents the segmentation performance of different algorithms on six transfer tasks between regular fundus datasets. It can be observed that the proposed method outperforms the baseline method in all metrics, which demonstrates the need for domain adaptation in the presence of large differences between domains. In addition, our proposed method achieves better segmentation performance compared to other adversarial learning methods (DANN,AdaptSeg,AMCD), suggesting that the traditional BN layer may not be applicable to the domain adaptation problem and that directly combining features from the source and target domains for normalization deteriorates the transferability of the network. Finally, the proposed method achieves further performance improvement over AdaBN and DSBN, which indicates that each feature channel may capture different patterns and our method is able to further improve the generalization performance of the network by reweighting each feature channel.

Fig. 4 visualizes the segmentation results of different algorithms on transfer tasks between regular fundus datasets. From top to bottom are the segmentation results for the transfer tasks *DRIVE*  $\rightarrow$  *STARE*, *STARE*  $\rightarrow$  *DRIVE*, *DRIVE*  $\rightarrow$  *Retinal40*, respectively, and the local patches of retinal vessels with different vessel widths are enlarged and shown on the right of each subfigure. It can be found that the proposed method can identify most of the retinal vessels, including those in low contrast and low light conditions. In addition, the proposed method is able to maintain the morphological structure of the vessels well, including the branches of the vessels, the vessel tree, and the edges of the vessels, etc.

TABLE I

SEGMENTATION PERFORMANCE OF DIFFERENT ALGORITHMS ON THE TRANSFER TASKS BETWEEN REGULAR FUNDUS DATASETS AND UWF FUNDUS DATASETS

Method	AUC	AUPR	F1	SE	SP	ACC
Baseline	0.9600	0.6883	0.5224	0.3606	0.9934	0.9836
DANN [23]	0.9625	0.6950	0.5550	0.4149	0.9953	0.9860
AdaptSeg [22]	0.9667	0.6965	0.5785	0.4385	0.9962	0.9861
AdaBN [28]	0.9720	0.7301	0.6588	0.6091	0.9939	0.9853
AMCD [24]	0.9706	0.7015	0.5973	0.4581	0.9992	0.9865
DSBN [29]	0.9722	0.7523	0.6974	0.6168	<b>0.9993</b>	0.9863
<b>Proposed</b>	<b>0.9778</b>	<b>0.7707</b>	<b>0.7143</b>	<b>0.6375</b>	0.9989	<b>0.9883</b>
Baseline	0.9601	0.7190	0.6449	0.5301	0.9883	0.9769
DANN [23]	0.9747	0.7234	0.6628	0.5429	0.9975	0.9874
AdaptSeg [22]	0.9759	0.7336	0.6745	0.5578	0.9977	0.9875
AdaBN [28]	0.9781	0.7561	0.6841	0.5774	<b>0.9979</b>	0.9877
AMCD [24]	0.9780	0.7451	0.6814	0.5616	0.9973	0.9872
DSBN [29]	0.9784	0.7628	0.6856	0.5898	0.9978	0.9879
<b>Proposed</b>	<b>0.9811</b>	<b>0.7810</b>	<b>0.7107</b>	<b>0.6209</b>	0.9953	<b>0.9881</b>
Baseline	0.9701	0.7568	0.6219	0.4623	0.9894	0.9821
DANN [23]	0.9768	0.7616	0.6503	0.5442	0.9939	0.9836
AdaptSeg [22]	0.9776	0.7742	0.6596	0.5936	0.9941	0.9850
AdaBN [28]	0.9787	0.7843	0.6685	0.6099	0.9954	0.9866
AMCD [24]	0.9785	0.7765	0.6672	0.6017	0.9949	0.9850
DSBN [29]	0.9788	0.7830	0.7028	0.6258	0.9959	0.9867
<b>Proposed</b>	<b>0.9869</b>	<b>0.8088</b>	<b>0.7309</b>	<b>0.6634</b>	<b>0.9964</b>	<b>0.9888</b>

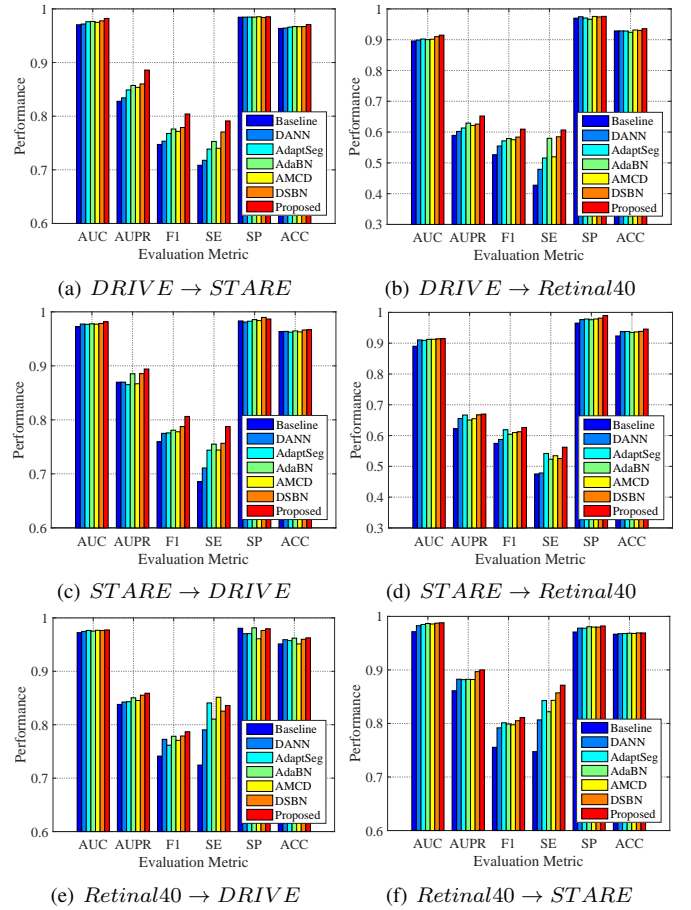


Fig. 3. Segmentation performance of different algorithms on transfer tasks between regular fundus datasets.

2) *Evaluations on the Transfer Tasks Regular  $\rightarrow$  UWF*: To further validate the effectiveness of the proposed algorithm, we also conducted experiments on the transfer task between the regular fundus dataset and the UWF fundus dataset, which is a more challenging task because along with contrast, lighting conditions, and lesions, the UWF images also have a larger field of view and higher resolution compared to the regular fundus images. The segmentation performance of different algorithms on three transfer tasks *DRIVE*  $\rightarrow$  *UWF*, *STARE*  $\rightarrow$  *UWF*, and *Retinal40*  $\rightarrow$  *UWF* are listed in the second row, third row and fourth row of Tabel I, respectively. It can be found that the proposed method outperforms other six comparison methods in almost all metrics on the three transfer tasks. Our method achieves the highest average AUC of 0.9819, the highest average AUPR of 0.7868, the highest average F1 of 0.7186, the highest sensitivity of 0.6406, and the highest accuracy of 0.9884, which yield performance improvements of 0.55%, 2.08%, 2.34%, 2.98%, and 0.14%, respectively, compared to the best comparison algorithm DSBN. This suggests that despite the greater variations between UWF fundus images and regular fundus images, our method still has better discriminatory ability for vessels and is able to detect more vessels than other methods.

Fig. 5 visualizes the segmentation results of different algorithms on the transfer task *Retinal40*  $\rightarrow$  *UWF*. Two enlarged



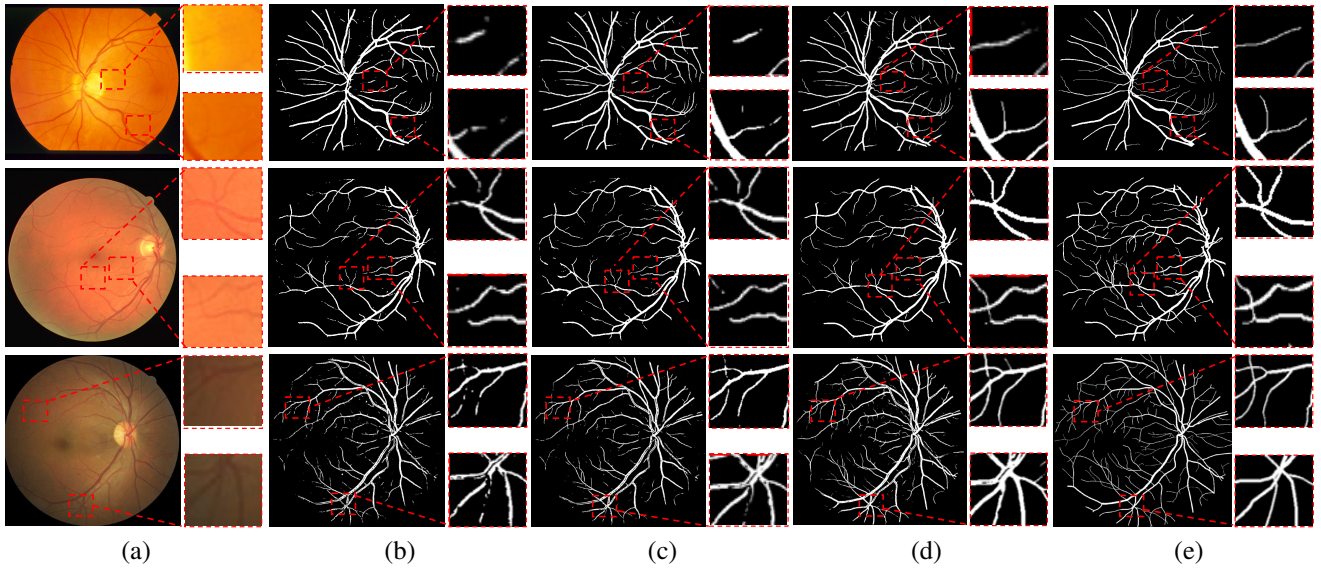


Fig. 4. Visualization of segmentation results of different algorithms on the transfer tasks between regular fundus datasets. (a) Original image; (b) Baseline; (c) DSBN [29]; (d) Proposed; (e) Ground Truth. From top to bottom are the transfer tasks  $DRIVE \rightarrow STARE$ ,  $STARE \rightarrow DRIVE$ ,  $DRIVE \rightarrow Retinal40$ , respectively. Two enlarged fundus image patches are shown on the right of each subfigure.

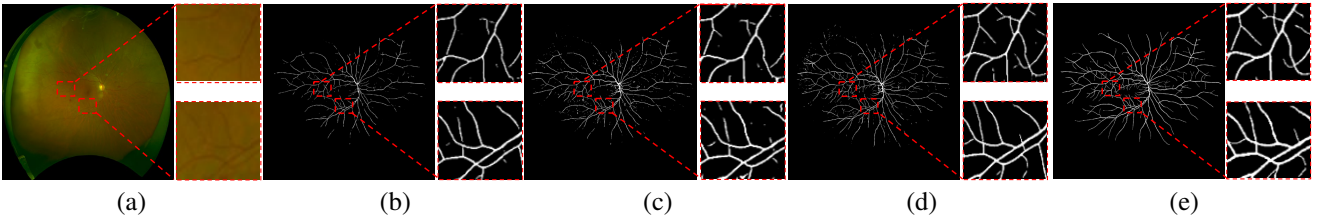


Fig. 5. Visualization of segmentation results of different algorithms on the transfer task  $Retinal40 \rightarrow UWF$ . (a) Original image; (b) Baseline; (c) DSBN [29]; (d) Proposed; (e) Ground Truth. Two enlarged fundus image patches are shown on the right of each subfigure.

local fundus regions are shown on the right of each subfigure. It can be observed that segmentation models trained on regular fundus data have difficulty detecting blood vessels in the posterior pole of the retina due to differences in imaging range; DSBN is able to detect more blood vessels in the posterior pole, because it uses domain-specific normalization layer to compensate for domain gaps. Our method is able to select the more transferable feature channels by reweighting each feature channel, thus allowing better detection of vessels in the retina while maintaining the morphological structure of the vessels in the UWF fundus images.

#### D. Ablation Study

Our approach consists of two key components: **entropy-based adversarial learning** and **transfer normalization**. Here we conduct ablation studies to verify the effectiveness of each component. We compare our approach with (1) the baseline model; (2) using only entropy-based adversarial learning (EA in Tabel II); and (3) using only transfer normalization (TN in Tabel II). As shown in Tabel II, both entropy-based adversarial learning and transfer normalization can bring performance improvements for cross-domain retinal vessel segmentation. Compared with the baseline model, the AUPR of EA and TN improved by 1.8% and 2.99%, respectively. It is worth noting that our proposed method achieves better performance by combining these two key components.

TABLE II  
ABLATION STUDY ON DIFFERENT COMPONENTS

Method	AUC	AUPR	F1	SE	SP	ACC
Baseline	0.9701	0.7568	0.6219	0.4623	0.9894	0.9821
EA	0.9779	0.7748	0.6636	0.6036	0.9901	0.9850
TN	0.9792	0.7867	0.7122	0.6303	<b>0.9969</b>	0.9876
<b>Proposed</b>	<b>0.9869</b>	<b>0.8088</b>	<b>0.7309</b>	<b>0.6634</b>	0.9964	<b>0.9888</b>

#### E. Channel Visualization

The weight  $\eta$  calculated in Eq. (7) quantify the transferability of the different feature channels, and a larger weight means that the feature channel is more transferable and therefore is given higher importance. Here, we visualize some feature channels. As shown in Fig. 6, it can be observed that certain feature channels are given a larger weight, e.g.,  $\eta$  of 0.89 for channel 23, due to the fact that this feature channel captures domain-shared features, e.g., the texture of blood vessels; while certain channels are given a smaller weight, e.g.,  $\eta$  of 0.26 for channel 16, due to the fact that these feature channels capture non-essential domain-specific patterns, e.g., backgrounds, lesions, etc.

#### F. Discussion

1) *Different Distance Type and Different Probability Type*: In our transfer normalization, in order to quantify the transferability of the different feature channels, we first calculate the



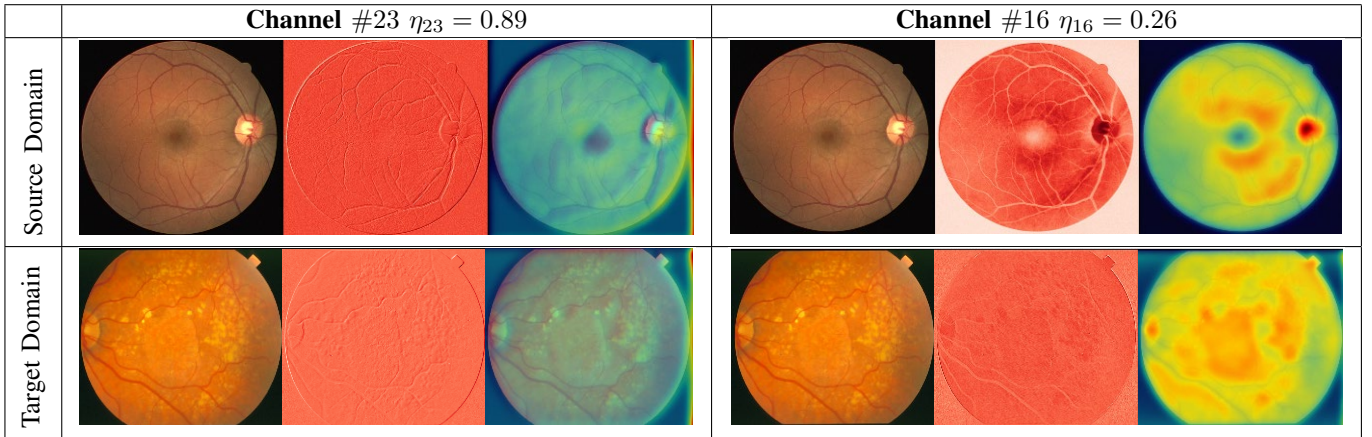


Fig. 6. Visualization of the transferability of different feature channels. In each group, the left is the original image, the middle is the feature channel, and the right is the result of combining the feature channel and the original image.

distances between the different feature channels by Eq. (6), and then convert the calculated distances into probability values by Eq. (7) to re-weight each feature channel. Here, we consider different types of distances: mean-based distance, Wasserstein Distance ( $\|E[h_m^s] - E[h_m^t]\|_2^2 + ((\text{Var}[h_m^s])^2 + (\text{Var}[h_m^t])^2 - 2\text{Var}[h_m^s]\text{Var}[h_m^t]))$ ), and our method. We conducted experiments on the transfer task *Retinal40*  $\rightarrow$  *UWF*. As shown in Tabel III, the mean-based distance does not take into account the variance, while the Wasserstein Distance cannot balance the importance of the mean and the variance. Our method uses the mean normalized by variance, which is similar to BN, and yields the best performance. In addition, we compared three probability types: Softmax, Gaussian, and Student-t distribution. As shown in Tabel III, better generalization performance was achieved using the Student-t distribution because it has a heavier tail and therefore it is able to emphasize the more transferable feature channels while avoiding over-punishing the other channels.

TABLE III

SEGMENTATION PERFORMANCE OF OUR METHOD USING DIFFERENT DISTANCE TYPES AND DIFFERENT PROBABILITY TYPES

Method	Different distance types			Different probability types		
	$E[h_m]$	Wasserstein Distance	$\frac{E[h_m]}{\sqrt{\text{Var}[h_m]+\epsilon}}$	Softmax	Gaussian	Student-t
AUC	0.9822	0.9855	<b>0.9869</b>	0.9834	0.9859	<b>0.9869</b>
AUPR	0.7833	0.7953	<b>0.8088</b>	0.7918	0.7985	<b>0.8088</b>
F1	0.7123	0.7156	<b>0.7309</b>	0.7192	0.7241	<b>0.7309</b>
SE	0.6421	0.6542	<b>0.6634</b>	0.6572	0.6592	<b>0.6634</b>
SP	0.9945	<b>0.9971</b>	0.9964	<b>0.9964</b>	0.9953	<b>0.9964</b>
ACC	0.9821	0.9829	<b>0.9888</b>	0.9863	0.9872	<b>0.9888</b>

2) *Connection to Entropy Minimization Principle*: [20] proposed to apply the entropy minimization principle to the domain adaptation setting to adjust the model to pass through low-density region of unlabeled target domain data, so that the model can make highly confident predictions on target domain data. The entropy-based adversarial learning in our approach can be seen as an indirect entropy minimization. As shown in Fig. 7(a),(b), due to domain shift, the entropy maps of the source and target domains have a large difference in distribution, where the entropy map of the source domain is clear (certain, low-entropy) while that of the target domain is

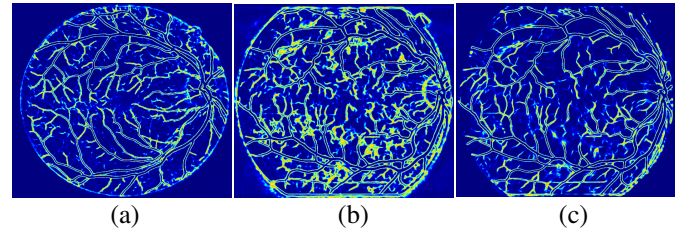


Fig. 7. Visualization of entropy maps. (a) entropy map on the source domain fundus dataset; (b) entropy map produced by the baseline method on the target domain fundus image; (c) entropy map produced by our method on the target domain fundus image.

noisy (uncertain, high-entropy). Our proposed method aligns the distribution of the entropy maps of the source and target domains by using adversarial learning, thus encouraging the model to be able to produce highly confident predictions even on unlabeled target domain data (see Fig. 7(c)). Furthermore, our approach and the entropy minimization principle are complementary. Here, we conducted experiments on the transfer task *Retinal40*  $\rightarrow$  *UWF*. As shown in Tabel IV, incorporating entropy minimization principle (MinEnt) into our proposed method yields better segmentation performance.

TABLE IV

SEGMENTATION PERFORMANCE OF OUR PROPOSED METHOD AND OUR PROPOSED METHOD WITH MINENT

Method	AUC	PR	F1	SE	SP	ACC
Proposed	0.9869	0.8088	0.7309	0.6634	<b>0.9964</b>	0.9888
Proposed+MinEnt [20]	<b>0.9871</b>	<b>0.8093</b>	<b>0.7321</b>	<b>0.6642</b>	<b>0.9964</b>	<b>0.9891</b>

## V. CONCLUSION

In this paper, we propose a new deep unsupervised domain adaptation framework for cross-domain retinal vessel segmentation. Using our proposed entropy-based adversarial learning and transfer normalization layer, we can train a segmentation model to be able to generalize well across fundus datasets from different domains, without requiring any ground truth labels for fundus images in the target domain. Extensive experiments on regular fundus datasets and UWF fundus dataset validate the effectiveness of the proposed approach. Our approach not

only brings a new idea for unsupervised domain adaption in retinal vessel segmentation, but also presents an innovative approach that can potentially be used for other cross-domain medical image segmentation tasks.

## REFERENCES

- [1] C. L. Srinidhi, P. Aparna, and J. Rajan, "Recent advancements in retinal vessel segmentation," *Journal of medical systems*, vol. 41, no. 4, p. 70, 2017.
- [2] N. Patton, T. Aslam, T. MacGillivray, A. Pattie, I. J. Deary, and B. Dhillon, "Retinal vascular image analysis as a potential screening tool for cerebrovascular disease: a rationale based on homology between cerebral and retinal microvasculatures," *Journal of anatomy*, vol. 206, no. 4, pp. 319–348, 2005.
- [3] Q. Jin, Z. Meng, T. D. Pham, Q. Chen, L. Wei, and R. Su, "Dunet: A deformable network for retinal vessel segmentation," *Knowledge-Based Systems*, vol. 178, pp. 149–162, 2019.
- [4] S. Lian, L. Li, G. Lian, X. Xiao, Z. Luo, and S. Li, "A global and local enhanced residual u-net for accurate retinal vessel segmentation," *IEEE/ACM transactions on computational biology and bioinformatics*, 2019.
- [5] Y. Wu, Y. Xia, Y. Song, Y. Zhang, and W. Cai, "Multiscale network followed network model for retinal vessel segmentation," in *International Conference on Medical Image Computing and Computer-Assisted Intervention*. Springer, 2018, pp. 119–126.
- [6] L. Ding, A. E. Kuriyan, R. S. Ramchandran, C. C. Wykoff, and G. Sharma, "Weakly-supervised vessel detection in ultra-widefield fundus photography via iterative multi-modal registration and learning," *IEEE Transactions on Medical Imaging*, 2020.
- [7] L. Ju, X. Wang, X. Zhao, P. Bonnington, T. Drummond, and Z. Ge, "Leveraging regular fundus images for training uwf fundus diagnosis models via adversarial learning and pseudo-labeling," *IEEE Transactions on Medical Imaging*, 2021.
- [8] S. J. Pan and Q. Yang, "A survey on transfer learning," *IEEE Transactions on knowledge and data engineering*, vol. 22, no. 10, pp. 1345–1359, 2009.
- [9] C. E. Shannon, "A mathematical theory of communication," *The Bell system technical journal*, vol. 27, no. 3, pp. 379–423, 1948.
- [10] M. Al-Rawi, M. Qutaishat, and M. Arrar, "An improved matched filter for blood vessel detection of digital retinal images," *Computers in biology and medicine*, vol. 37, no. 2, pp. 262–267, 2007.
- [11] O. Wink, W. J. Niessen, and M. A. Viergever, "Multiscale vessel tracking," *IEEE Transactions on Medical Imaging*, vol. 23, no. 1, pp. 130–133, 2004.
- [12] M. M. Fraz, P. Remagnino, A. Hoppe, B. Uyyanonvara, C. G. Owen, A. R. Rudnicka, and S. Barman, "Retinal vessel extraction using first-order derivative of gaussian and morphological processing," in *International Symposium on Visual Computing*. Springer, 2011, pp. 410–420.
- [13] S. Moccia, E. De Momi, S. El Hadji, and L. S. Mattos, "Blood vessel segmentation algorithms—review of methods, datasets and evaluation metrics," *Computer methods and programs in biomedicine*, vol. 158, pp. 71–91, 2018.
- [14] J. V. Soares, J. J. Leandro, R. M. Cesar, H. F. Jelinek, and M. J. Cree, "Retinal vessel segmentation using the 2-d gabor wavelet and supervised classification," *IEEE Transactions on medical Imaging*, vol. 25, no. 9, pp. 1214–1222, 2006.
- [15] S. Roychowdhury, D. D. Koozekanani, and K. K. Parhi, "Blood vessel segmentation of fundus images by major vessel extraction and subimage classification," *IEEE journal of biomedical and health informatics*, vol. 19, no. 3, pp. 1118–1128, 2014.
- [16] Z. Yan, X. Yang, and K.-T. Cheng, "Joint segment-level and pixel-wise losses for deep learning based retinal vessel segmentation," *IEEE Transactions on Biomedical Engineering*, vol. 65, no. 9, pp. 1912–1923, 2018.
- [17] J. Son, S. J. Park, and K.-H. Jung, "Retinal vessel segmentation in fundoscopic images with generative adversarial networks," *arXiv preprint arXiv:1706.09318*, 2017.
- [18] X. Sun, X. Cao, Y. Yang, L. Wang, and Y. Xu, "Robust retinal vessel segmentation from a data augmentation perspective," *arXiv preprint arXiv:2007.15883*, 2020.
- [19] X. Peng, Q. Bai, X. Xia, Z. Huang, K. Saenko, and B. Wang, "Moment matching for multi-source domain adaptation," in *Proceedings of the IEEE/CVF International Conference on Computer Vision*, 2019, pp. 1406–1415.
- [20] M. Long, Y. Cao, Z. Cao, J. Wang, and M. I. Jordan, "Transferable representation learning with deep adaptation networks," *IEEE transactions on pattern analysis and machine intelligence*, vol. 41, no. 12, pp. 3071–3085, 2018.
- [21] I. Goodfellow, J. Pouget-Abadie, M. Mirza, B. Xu, D. Warde-Farley, S. Ozair, A. Courville, and Y. Bengio, "Generative adversarial nets," *Advances in neural information processing systems*, vol. 27, 2014.
- [22] Y.-H. Tsai, W.-C. Hung, S. Schuler, K. Sohn, M.-H. Yang, and M. Chandraker, "Learning to adapt structured output space for semantic segmentation," in *Proceedings of the IEEE conference on computer vision and pattern recognition*, 2018, pp. 7472–7481.
- [23] M. Javanmardi and T. Tasdizen, "Domain adaptation for biomedical image segmentation using adversarial training," in *2018 IEEE 15th International Symposium on Biomedical Imaging (ISBI 2018)*. IEEE, 2018, pp. 554–558.
- [24] J. Zhuang, Z. Chen, J. Zhang, D. Zhang, and Z. Cai, "Domain adaptation for retinal vessel segmentation using asymmetrical maximum classifier discrepancy," in *Proceedings of the ACM Turing Celebration Conference-China*, 2019, pp. 1–6.
- [25] S. Ioffe and C. Szegedy, "Batch normalization: Accelerating deep network training by reducing internal covariate shift," in *International conference on machine learning*. PMLR, 2015, pp. 448–456.
- [26] S. Santurkar, D. Tsipras, A. Ilyas, and A. Madry, "How does batch normalization help optimization?" *Advances in Neural Information Processing Systems*, vol. 31, 2018.
- [27] J. Quionero-Candela, M. Sugiyama, A. Schwaighofer, and N. D. Lawrence, "Dataset shift in machine learning. the mit press," 2009.
- [28] Y. Li, N. Wang, J. Shi, J. Liu, and X. Hou, "Revisiting batch normalization for practical domain adaptation," *arXiv preprint arXiv:1603.04779*, 2016.
- [29] Q. Liu, Q. Dou, L. Yu, and P. A. Heng, "Ms-net: multi-site network for improving prostate segmentation with heterogeneous mri data," *IEEE transactions on medical imaging*, vol. 39, no. 9, pp. 2713–2724, 2020.
- [30] Student, "The probable error of a mean," *Biometrika*, pp. 1–25, 1908.
- [31] K. He, X. Zhang, S. Ren, and J. Sun, "Deep residual learning for image recognition," in *Proceedings of the IEEE conference on computer vision and pattern recognition*, 2016, pp. 770–778.
- [32] J. Staal, M. D. Abràmoff, M. Niemeijer, M. A. Viergever, and B. Van Ginneken, "Ridge-based vessel segmentation in color images of the retina," *IEEE transactions on medical imaging*, vol. 23, no. 4, pp. 501–509, 2004.
- [33] A. Hoover, V. Kouznetsova, and M. Goldbaum, "Locating blood vessels in retinal images by piecewise threshold probing of a matched filter response," *IEEE Transactions on Medical imaging*, vol. 19, no. 3, pp. 203–210, 2000.
- [34] J. Schindelin, I. Arganda-Carreras, E. Frise, V. Kaynig, M. Longair, T. Pietzsch, S. Preibisch, C. Rueden, S. Saalfeld, B. Schmid *et al.*, "Fiji: an open-source platform for biological-image analysis," *Nature methods*, vol. 9, no. 7, pp. 676–682, 2012.
- [35] L. Ding, A. Kuriyan, R. Ramchandran, C. Wykoff, and G. Sharma, "Prime-fp20: Ultra-widefield fundus photography vessel segmentation dataset," *IEEE Dataport*, 2020.
- [36] A. W. Setiawan, T. R. Mengko, O. S. Santoso, and A. B. Sukmono, "Color retinal image enhancement using clahe," in *International Conference on ICT for Smart Society*. IEEE, 2013, pp. 1–3.
- [37] O. Ronneberger, P. Fischer, and T. Brox, "U-net: Convolutional networks for biomedical image segmentation," in *International Conference on Medical image computing and computer-assisted intervention*. Springer, 2015, pp. 234–241.
- [38] A. Radford, L. Metz, and S. Chintala, "Unsupervised representation learning with deep convolutional generative adversarial networks," *arXiv preprint arXiv:1511.06434*, 2015.
- [39] D. P. Kingma and J. Ba, "Adam: A method for stochastic optimization," *arXiv preprint arXiv:1412.6980*, 2014.
- [40] L.-C. Chen, G. Papandreou, I. Kokkinos, K. Murphy, and A. L. Yuille, "Deepplab: Semantic image segmentation with deep convolutional nets, atrous convolution, and fully connected crfs," *IEEE transactions on pattern analysis and machine intelligence*, vol. 40, no. 4, pp. 834–848, 2017.
- [41] A. Paszke, S. Gross, S. Chintala, G. Chanan, E. Yang, Z. DeVito, Z. Lin, A. Desmaison, L. Antiga, and A. Lerer, "Automatic differentiation in pytorch," 2017.